nature communications

Article

https://doi.org/10.1038/s41467-025-58487-x

Electron correlation and incipient flat bands in the Kagome superconductor $CsCr_3Sb_5$

Received: 4 October 2024

Accepted: 25 March 2025

Published online: 04 April 2025

Check for updates

Yidian Li[1,12], Yi Liu[2,3,12], Xian Du[1,12], Siqi Wu[2], Wenxuan Zhao[1], Kaiyi Zhai[1], Yinqi Hu[1], Senyao Zhang[1], Houke Chen[4], Jieyi Liu[4], Yiheng Yang[4], Cheng Peng[4], Makoto Hashimoto[5], Donghui Lu[5], Zhongkai Liu[6,7], Yilin Wang[8,9,10] ✉, Yulin Chen[4,6,7] ✉, Guanghan Cao[2] ✉ & Lexian Yang[1,11] ✉

Correlated kagome materials exhibit a compelling interplay between lattice geometry, electron correlation, and topology. In particular, the flat bands near the Fermi level provide a fertile playground for novel many-body states. Here we investigate the electronic structure of $CsCr_3Sb_5$ using high-resolution angle-resolved photoemission spectroscopy and ab-initio calculations. Our results suggest that Cr 3*d* electrons are intrinsically incoherent, showing strong electron correlation amplified by Hund's coupling. Notably, we identify incipient flat bands close to the Fermi level, which are expected to significantly influence the electronic properties of the system. Across the density-wave-like transition at 55 K, we observe a drastic enhancement of the electron scattering rate, which aligns with the semiconducting-like property at high temperatures. These findings establish $CsCr_3Sb_5$ as a strongly correlated Hund's metal with incipient flat bands near the Fermi level, which provides an electronic basis for understanding its novel properties compared to the weakly correlated AV_3Sb_5.

Kagome materials with corner-sharing triangular networks in their lattice structures exhibit rich and fascinating properties, such as spin liquid states[1–3], topological quantum phases[4–8], fractional quantum Hall effect[9–11], and many-body emergent phenomena[12–15]. The characteristic electronic structure of a typical kagome lattice includes the flat band, the Dirac fermions at the *K* point, and the van Hove singularity (vHS) at the *M* point (Fig. 1a). If the Fermi level (E_F) is tuned to the flat band, novel magnetic states such as fractional quantum Hall effect and quantum anomalous Hall effect may emerge, while the vHS and the Dirac fermions at the E_F can induce unconventional superconductivity, charge-density wave (CDW), and/or other novel properties[16–18]. Up to date, many different kagome materials with characteristic kagome electronic structures have been discovered and extensively studied[5,8,18–22]. However, the investigation of intrinsic kagome-related many-body ground states remains inadequate since the flat bands are usually situated far from E_F, and their impact on the electronic properties of the system requires further exploration.

Among the abundant kagome materials, AV_3Sb_5 (*A* = K, Rb, and Cs) have attracted great attention due to their intriguing emergent properties[15,23], such as the interplay/competition between unconventional superconductivity and CDW[12–15], time- and/or rotational-symmetry broken phases[24–31], giant anomalous Hall effect related to

[1]State Key Laboratory of Low Dimensional Quantum Physics, Department of Physics, Tsinghua University, Beijing, China. [2]School of Physics, Zhejiang University, Hangzhou, China. [3]Department of Applied Physics, Key Laboratory of Quantum Precision Measurement of Zhejiang Province, Zhejiang University of Technology, Hangzhou, China. [4]Department of Physics, Clarendon Laboratory, University of Oxford, Oxford, UK. [5]Stanford Synchrotron Radiation Lightsource, SLAC National Accelerator Laboratory, Menlo Park, CA, USA. [6]School of Physical Science and Technology, ShanghaiTech University and CAS-Shanghai Science Research Center, Shanghai, China. [7]ShanghaiTech Laboratory for Topological Physics, Shanghai, China. [8]School of Emerging Technology, University of Science and Technology of China, Hefei, China. [9]New Cornerstone Science Laboratory, University of Science and Technology of China, Hefei, China. [10]Hefei National Laboratory, University of Science and Technology of China, Hefei, China. [11]Collaborative Innovation Center of Quantum Matter, Beijing, China. [12]These authors contributed equally: Yidian Li, Yi Liu, Xian Du. ✉e-mail: yilinwang@ustc.edu.cn; yulin.chen@physics.ox.ac.uk; ghcao@zju.edu.cn; lxyang@tsinghua.edu.cn

https://doi.org/10.1038/s41467-025-58487-x

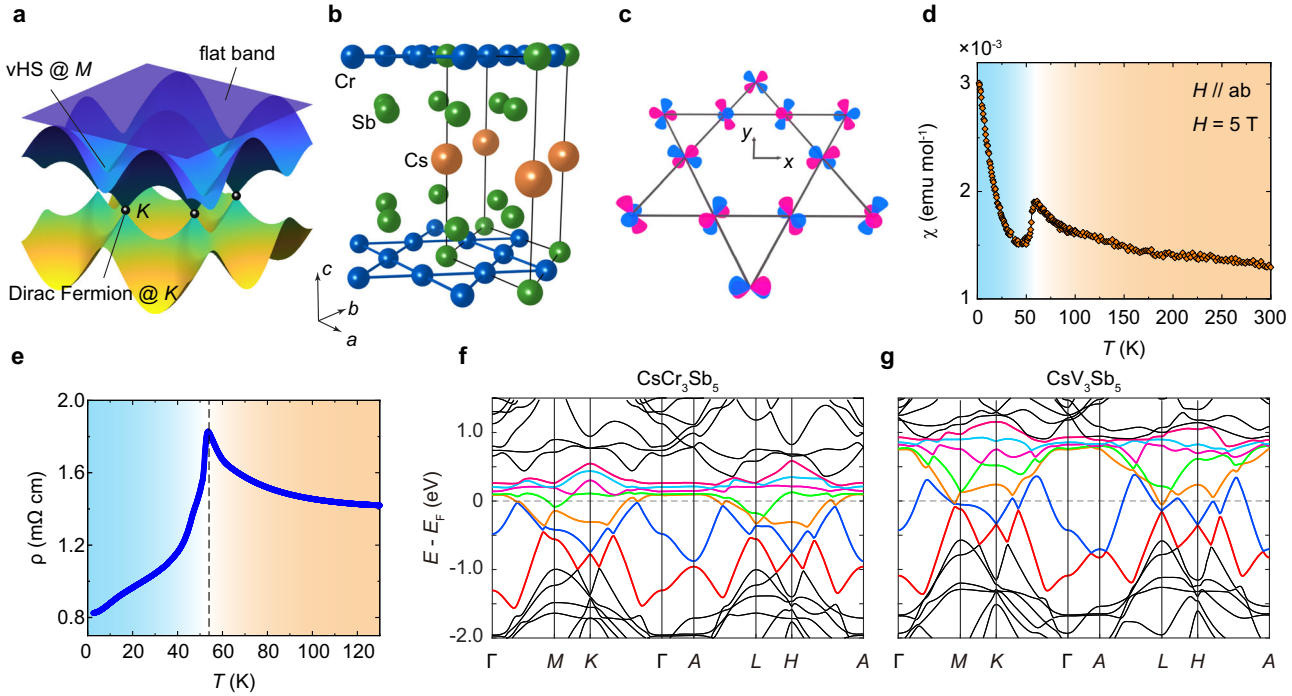

Fig. 1 | Basic properties of $CsCr_3Sb_5$. a Schematic illustration of the characteristic band structure of a kagome lattice including the flat band, the Dirac fermion at the *K* point, and the van Hove singularity (vHS) at the *M* point. **b** The crystal structure of $CsCr_3Sb_5$ in which Cr atoms form a planar kagome lattice. **c** Kagome structure of Cr *d* orbitals. For simplicity, only the d_{xz} orbital is shown. **d** In-plane magnetic susceptibility (χ) as a function of temperature measured at $H = 5$ T. **e** In-plane resistivity (ρ) as a function of temperature shows a peak near 55 K. **f**, **g** Comparison between the calculated band structure of $CsCr_3Sb_5$ (**f**) and CsV_3Sb_5 (**g**) by the density functional theory (DFT). The colored lines indicate similar dispersions of the two materials.

the chirality of the charge order[27,32], the observation of pair-density waves[33,34], and putative loop current order[35–37]. In the exploration of AV_3Sb_5 materials, it has been a common consensus that the vHS near E_F plays a key role in the CDW and possibly also in the superconductivity[38,39], while the attractive flat band was observed far away from E_F[40].

Moreover, the non-magnetic and weakly correlated kagome physics of AV_3Sb_5 can be further enriched by introducing magnetism and strong electron correlations. By replacing vanadium with chromium, the sibling compound $CsCr_3Sb_5$ provides an ideal platform to investigate the impact of magnetism and electronic correlation effect in the AV_3Sb_5-type kagome systems[41]. Indeed, recent investigations reveal many novel properties of this new kagome material, including superconductivity up to 6.4 K under pressure, frustrated altermagnetism, density-wave-like order, and non-Fermi liquid behavior in the high-temperature state[41–43]. Compared to the non-magnetic and weakly correlated AV_3Sb_5, incipient flat bands (IFB, flat bands that extend in a small portion of Brillouin zone and locate away from E_F)[44] originated from correlated Cr 3*d* orbitals appear near E_F, which may dominate the correlated electronic properties of the system. These novel electronic characteristics, together with the prototypical kagome electronic structure of $CsCr_3Sb_5$, require systematic experimental studies of its electronic structure.

In this work, by performing high-resolution angle-resolved photoemission spectroscopy (ARPES) measurements, we systematically investigate the electronic structure of $CsCr_3Sb_5$ single crystals. Our experiments reveal weakly correlated Sb 5*p* states and intrinsically incoherent Cr 3*d* states, in overall agreement with our density functional theory (DFT) and dynamical mean-field theory (DMFT) calculations. Compared to CsV_3Sb_5, the vHSs and Dirac fermions characterizing the kagome lattice locate far away from E_F. Interestingly, we observe a flat Cr 3*d* band at about 80 meV below E_F, confirming the existence of IFB close to E_F. Moreover, the electron scattering rate, as manifested by the spectral broadening, is drastically enhanced above the density-wave transition temperature (~ 55 K), which is related to the semiconducting-like behavior of the system at high temperatures. These findings, in good consistency with the theoretical calculations[45,46], identify $CsCr_3Sb_5$ as a strongly correlated Hund's metal with IFB. Our work provides a foundation for further exploration of the correlated kagome material with unconventional superconductivity.

Results and discussion

Basic electronic structure of $CrCr_3Sb_5$

$CsCr_3Sb_5$ crystallizes in a similar layered structure of AV_3Sb_5 with the space group of *P*6/mmm (Fig. 1b)[41]. In each unit cell, the Cr atoms constitute a two-dimensional kagome lattice with Sb atoms occupying the center of the hexagons. It is mainly the Cr 3*d* orbitals that form the kagome electronic states near E_F, as schematically shown in Fig. 1c. Previous X-ray scattering and nuclear magnetic resonance experiments revealed an intertwined CDW and spin-density wave (SDW) below 55 K[41]. Consistently, our susceptibility measurement suggests an antiferromagnetic transition at 55 K (Fig. 1d), accompanied by a semiconducting-like to metal transition in the resistivity measurement (Fig. 1e), which is a manifestation of the intertwined density-wave-like order in the system. Fig 1f, g compare the DFT-calculated electronic structure of $CsCr_3Sb_5$ and CsV_3Sb_5. In general, the two compounds show similar electronic structures characterizing the kagome lattice. Compared to CsV_3Sb_5, where the vHSs are close to E_F, the vHSs and Dirac fermions in $CrCr_3Sb_5$ locate further away from E_F, suggesting their relatively irrelevance in the novel transport properties. Prominently, compared to CsV_3Sb_5, the bandwidth of the dispersive bands near E_F is much smaller, and the flat bands located close to E_F in $CsCr_3Sb_5$ (Fig. 1f), which are believed to play a key role in the unconventional superconductivity[44,47,48].

Fig 2a shows the calculated three-dimensional Fermi surface (FS) of $CsCr_3Sb_5$. There is a nearly cylindrical electron pocket and two cylindrical hole pockets with similar volumes at $k_{||} = 0$ (the $\bar{\Gamma}$ point),

https://doi.org/10.1038/s41467-025-58487-x

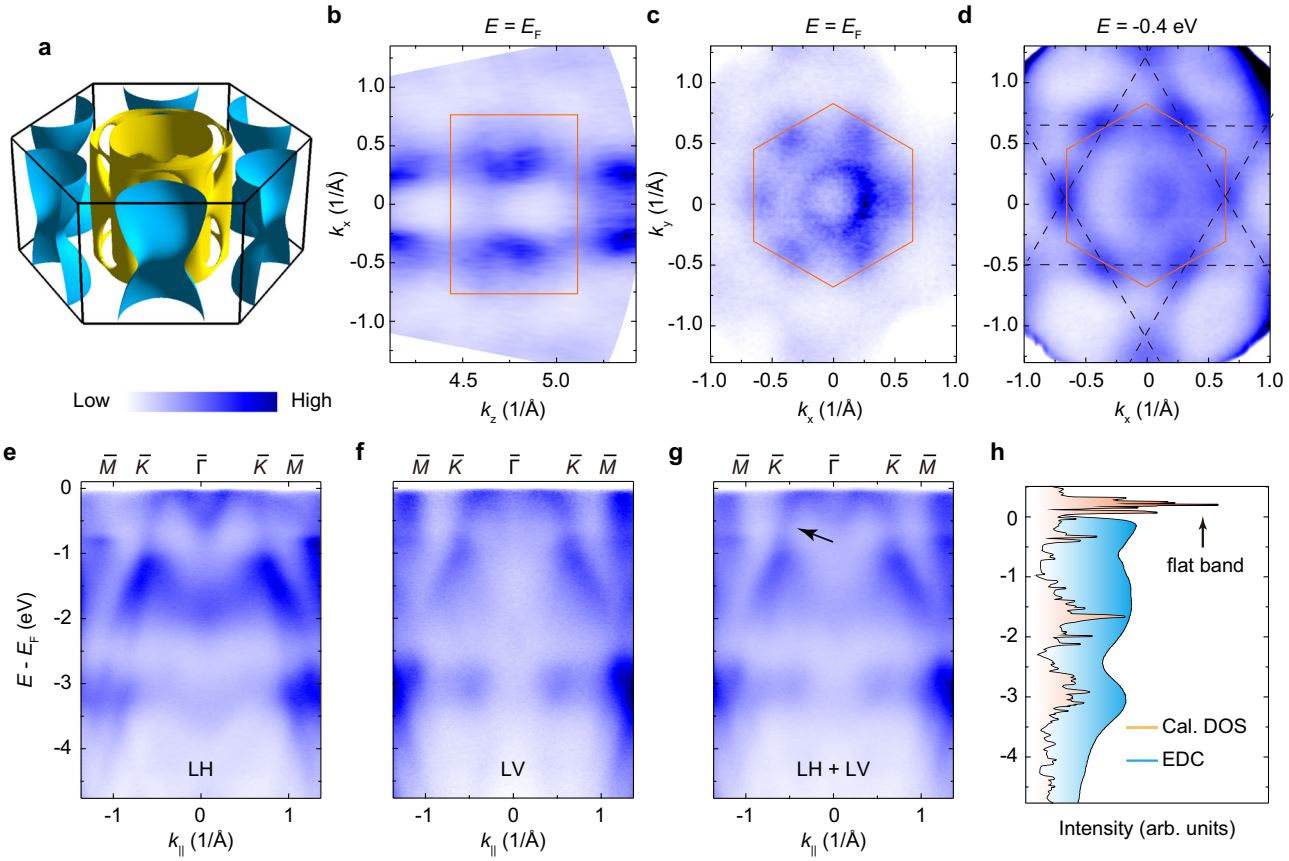

Fig. 2 | Overall band structures of $CsCr_3Sb_5$. a Three-dimensional plot of the calculated Fermi surface of $CsCr_3Sb_5$. **b** k_z dispersion measured in the photon energy range between 60 eV and 110 eV. **c**, **d** The k_x-k_y map of ARPES intensity at the Fermi level (E_F) and − 0.4 eV. **e**–**g** Band dispersion along $\bar{\Gamma}\bar{K}$ measured using different photon polarizations in a large energy range. The black arrow in (**g**) indicates the band that contributing to the star-of-David structure in (**d**). **h** Comparison between the calculated density-of-states (DOS) and integrated energy distribution curve (EDC). In panels (**c**, **d**, and **g**), the data measured with linear-horizontally (LH) and linear-vertically (LV) polarized photons were merged for completeness of the electronic structure. Data in (**c**–**g**) were measured using 93 eV photons. All data were collected at 6 K.

together with a warped cylindrical electron pocket around $k_{||} = 0.66$ Å^{-1} (the $\bar{M}$ point). At certain k_z, there is no Fermi crossing along $\bar{\Gamma}\bar{K}\bar{M}$, leaving holes in the cylindrical hole pockets around $\bar{\Gamma}$ (see the yellow Fermi pockets in Fig. 2a). The experimental FS in the k_x-k_z plane shows a weak but resolvable k_z dispersion of the bands around $k_{||} = 0$ (the $\bar{\Gamma}$ point), confirming the quasi-two-dimensionality of the electronic structure (Fig. 2b, also see the Supplementary Information). The FS in the k_x-k_y plane shows a hexagonal structure (Fig. 2c). We observe a circular electron pocket around the $\bar{\Gamma}$ point, together with a spectral-weight patch around the $\bar{M}$ point. With increasing binding energy, the circular electron pocket around the $\bar{\Gamma}$ point shrinks, and a star-of-David-shape pattern can be resolved at − 0.4 eV, as indicated by the black dashed lines in Fig. 2d.

Fig 2e–g shows the experimental band dispersions along high symmetry directions in a large energy range. Since the electronic states near E_F are mainly contributed by Cr 3*d* orbitals, the data strongly depend on the light polarization. In general, the spectra can be roughly divided into three segments in energy: the dispersive bands near E_F, an M-shape feature around − 1.5 eV, and weakly dispersive bands around − 3 eV. These features contribute peaks in the integrated energy distribution curve (EDC) that is in overall consistency with the calculated density-of-states (DOS), as compared in Fig. 2h.

Incipient Flat bands near E_F

Figure 3 shows the fine electronic structure along high-symmetry directions near E_F. The experiment shows an overall agreement with the calculation (Fig. 3a, b), as shown by the data overlaid with the renormalized calculation in the Supplementary Information. The energy bands originated from Sb *p* orbitals (Supplementary Information) are well captured by the calculation. Specifically, they form the vHS at the Γ point, which shows electron-like dispersion in the k_x-k_y plane and hole-like dispersion along k_z, as schematically shown in Fig. 3c. We notice that the electron band around $\bar{\Gamma}$ has mixed *p* and *d* orbital components, suggesting a *p*-*d* interaction (Supplementary Information). For the Cr 3*d* orbital bands, the spectra are generally much broader. It is noteworthy that while non-trivial surface states related to the Z_2 topological electronic structure were observed in AV_3Sb_5[40], here we do not find clear evidence for the surface states.

Prominently, we reveal a flat band close to E_F, as indicated by the red arrows in Fig. 3b. The flat band with a band bottom at about 80 meV below E_F can be better resolved from the data along $\bar{\Gamma}\bar{K}$ and the EDC at $\bar{\Gamma}$ shown in Fig. 3d (also see the Supplementary Information). This flat band close to E_F may play an important role in the transport properties of $CsCr_3Sb_5$ and contribute to the electronic specific-heat coefficient 105 mJ/(K·mol), much larger than CsV_3Sb_5[41]. The observation of the flat band in the ARPES experiment suggests that the DFT-calculated flat bands are pushed closer to E_F. To understand this difference, we perform DFT + DMFT calculation, which can better capture the strong electron correlations of Cr 3*d* electrons. The calculated spectral function at Coulomb interaction $U = 5$ eV and Hund's coupling $J_H = 0.88$ eV[45] is shown in Fig. 3e. Interestingly, the flat bands above E_F in Fig. 3a are indeed pushed closer to E_F and strongly renormalized, leaving the incipient flat band with prominent spectral weight mainly around the $\bar{\Gamma}$ point. It is likely that the E_F of $CsCr_3Sb_5$ crystals are

https://doi.org/10.1038/s41467-025-58487-x

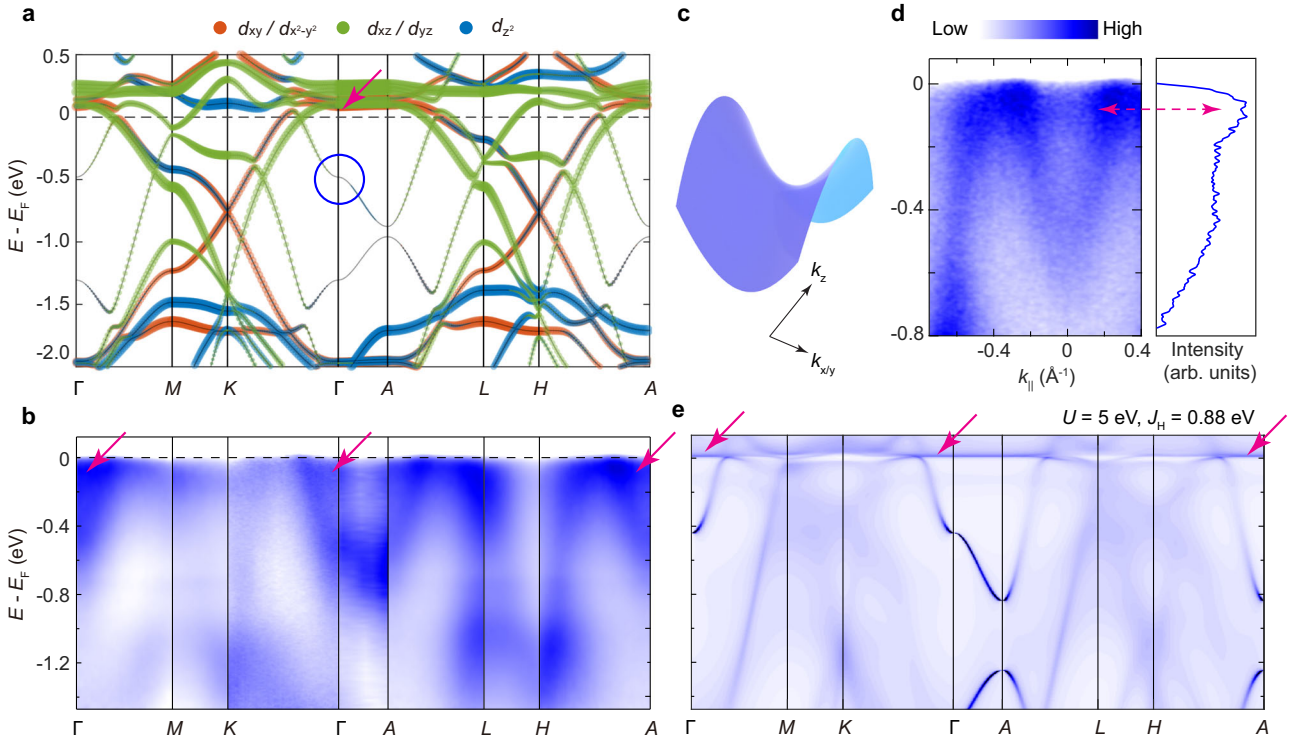

Fig. 3 | Comparison between experimental and calculated fine electronic structure of $CsCr_3Sb_5$ near E_F. a Density functional theory (DFT) calculation of the orbital-projected electronic structure of $CsCr_3Sb_5$ along high-symmetry directions. **b** ARPES spectra along high-symmetry directions. **c** Schematic illustration of the vHS at Γ (blue circle in **a**) with hole-like and electron-like dispersion along k_z and $k_{x/y}$, respectively. **d** Zoom-in plot of band dispersions along *AH* (left) and the corresponding EDC at *A* (right). **e** DFT + dynamical mean-field theory (DMFT) calculation of the electronic structure, with on-site Coulomb interaction $U = 5$ eV and Hund's coupling $J_H = 0.88$ eV. The red arrows indicate the flat band close to E_F (Supplementary Information). The calculated result with $U = 5$ eV and $J_H = 0.5$ eV is shown in the Supplementary Information. Data were collected at 6 K. For completeness, data measured with LH- and LV-polarized photons were merged.

slightly raised up by self-doping or surface effects and the flat bands, similar to the situation in CsV_3Sb_5[49]. Therefore, the flat band can be experimentally observed by the ARPES experiment.

Moreover, the DFT + DMFT calculation suggests that the electron correlation effect shows a minor impact on the Sb *p* orbital bands but strongly broadens Cr *d* orbital bands, well capturing the intrinsic characteristics of our ARPES spectra. We emphasize that the strong Hund's coupling is essential in understanding the strong renormalization of the effective mass and the enhanced electron self-energy[45]. As shown in the Supplementary Information, the calculation with different Hund's coupling suggests that the strong broadening of the Cr 3*d* orbitals are intrinsically due to the Hund's coupling. The agreement between our experiment and DMFT calculation thus confirms that $CsCr_3Sb_5$ is a strongly correlated Hund's metal with incipient flat bands.

Enhanced scattering rate across the density-wave-like transition

Although $CsCr_3Sb_5$ shows a density-wave-like transition near 55 K[41], as confirmed by our susceptibility and resistivity measurements, we did not observe clear signatures of band folding, splitting, or shift related to the transition with synchrotron-based ARPES (Fig. 4a and b). To better resolve the dispersion around the $\bar{\Gamma}$ point and track the temperature evolution of the band structure, we conducted laser-ARPES measurements with improved energy and momentum resolutions. The Sb *p* orbital band around $\bar{\Gamma}$ exhibits strong intensity with a slight change of the dispersion slope as approaching E_F, possibly due to the interaction with Cr 3*d* orbitals (Fig. 4c and the data after dividing the Fermi-Dirac distribution function in the Supplementary Information). Fig 4d shows the temperature evolution of our laser-ARPES spectra. Again, no clear change of the spectra, such as gap opening is observed across the density-wave transition at 55 K, as can be seen from the corresponding EDCs near E_F in Fig. 4e.

The metallic band structure, however, deviates from the observed semiconducting-like resistivity above 55 K. We notice that the spectra are suddenly broadened across the density-wave transition as shown by the MDCs near E_F (Fig. 4f). By fitting the MDCs of the Sb *p* orbital band at E_F to Lorentzians (black lines in Fig. 4f), we extract the full-width-at-half-maximum (FWHM) of the MDCs and plot the results as a function of temperature in Fig. 4g. Apparently, with increasing temperature, the FWHM quickly rises above about 50 K, suggesting an enhanced electron scattering rate at high temperatures, which is likely due to the enhanced fluctuation effect and may explain the semiconducting-like behavior of $CsCr_3Sb_5$ above 55 K. Further experimental and theoretical exploration are required to unravel the connection between the electronic structure and density-wave transition in this material.

Discussion

The replacement of vanadium by chromium greatly changes the electronic structure of AV_3Sb_5, making $CsCr_3Sb_5$ an ideal kagome material to explore correlated physics such as unconventional superconductivity and magnetism. On the one hand, the extra valance electrons in chromium raise the E_F of $CsCr_3Sb_5$ close to the flat bands compared to CsV_3Sb_5, leaving IFBs near E_F. On the other hand, the Coulomb interaction between Cr 3*d* electrons induces strong electron correlation, which is further enhanced by the Hund's coupling. Therefore, the scattering rate or the imaginary part of electron self-energy is greatly enhanced, making the electronic states intrinsically incoherent, as manifested by the broad ARPES spectra of Cr 3*d* electrons. We emphasize that only the Hubbard *U* cannot induce the experimentally observed large effective mass[41] and scattering rate (see

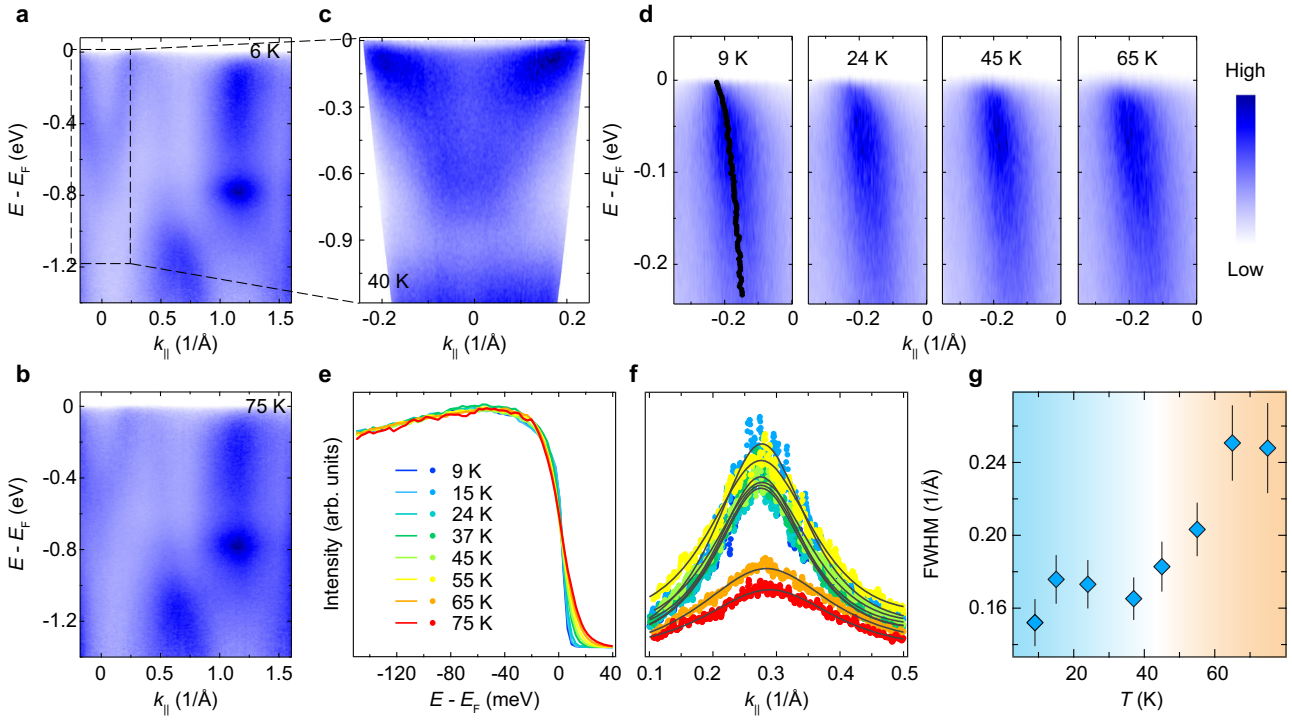

Fig. 4 | Temperature evolution of the electronic structure. a, **b** ARPES spectra measured at 6 K (**a**) and 75 K (**b**) with 52 eV photons. **c** Laser-ARPES spectra measured at 40 K showing the electron band around the $\bar{\Gamma}$ point. **d** Laser-ARPES spectra measured at different temperatures. The black line is the extracted band dispersion by fitting the momentum-distribution curves (MDCs) to Lorentzians. **e** EDCs at the Fermi momentum at different temperatures. **f** the MDCs at E_F at different temperatures with the fitting results overlaid. The corresponding temperatures are indicated in (**e**) (dots). **g** Temperature dependence of the full-width-at-half-maximum (FWHM) of the MDCs at E_F. Error bars represent the confidence intervals of the fitting under 95% confidence level. Data in (**c**–**g**) were collected using a 7 eV laser.

Figs. 3b, e, and the Supplementary Information), while the correlation effects are sensitive to the Hund's coupling[45], verifying $CsCr_3Sb_5$ as a strongly correlated Hund's metal.

The IFB and the strong electron correlation of $CsCr_3Sb_5$ provide an electronic basis for understanding its novel properties, such as large effective mass, magnetism, and unconventional superconductivity. Firstly, the cooperation of Hund's coupling and the IFBs significantly enhances the orbital-dependent electron correlation effect[45,46], similar to the physics in iron-based superconductors[50–52]. Moreover, the IFB can boost the Kondo-like effect, such as heavy fermion in Hund's metal, according to the previous theoretical calculation. It is, therefore, possible to tune the correlated physics of $CsCr_3Sb_5$ by controlling the portion and width of the IFBs[45]. Secondly, Hund's coupling induces the localization of the magnetic moments and intrinsically incoherent Cr 3*d* states. In the paramagnetic state, the fluctuation of local spin moments further enhances the scattering rate of electrons, as observed in our temperature-dependent measurements, which is related to the weak semiconducting-like transport property at high temperatures. With decreasing temperature, the system is expected to undergo an incoherence-to-coherence crossover by screening the local moments[45], and the relatively coherent flat bands can be observed near E_F, which is also consistent with our observation of the reduced scattering rate with decreasing temperature. Finally, the incipient flat band is believed to be crucial for unconventional superconductivity[44,47,48]. It has been shown that the application of pressure can effectively tune the portions and width of the incipient flat bands[45], which may be important for the pressurized superconductivity in $CsCr_3Sb_5$[41]. It is noteworthy that similar physics, including the flat bands near E_F, the correlation enhanced by Hund's coupling, and the competition between density-wave and pressurized superconductivity, has been revealed in the nickelates $La_{n+1}Ni_nO_{3n+1}$[53–56].

In summary, we systematically investigate the electronic structure of the correlated kagome material $CsCr_3Sb_5$. Our work reveals the characteristic electronic structure including the vHS and flat bands. The electronic scattering is drastically enhanced across the density-wave transition, providing an understanding of the semiconducting-like transport at high temperatures. Consistent with the DFT + DMFT calculations, our experimental results identify that $CsCr_3Sb_5$ is a strongly correlated Hund's metal with IFBs. Our work provides crucial information for understanding the novel properties of $CsCr_3Sb_5$ in comparison to the weakly-correlated and non-magnetic AV_3Sb_5 compounds.

Note: during the review process of the manuscript, we notice that several independent papers have investigated the electronic structures of $CsCr_3Sb_5$ and $Cs(V_{1-x}Cr_x)_3Sb_5$ with consistent results[57–59].

METHODS

Sample growth and characterization

Single crystals of $CsCr_3Sb_5$ were grown via a self-flux method. The details of the crystal growth can be seen in ref. 41. Hexagonal-shaped crystalline flakes with a typical size of $0.5 \times 0.5 \times 0.02$ mm^3 were harvested for the ARPES measurement. Before the ARPES experiment, crystals from the same batch were characterized by X-ray diffraction, energy-dispersive X-ray spectroscopy, and measurements of electrical resistivity and magnetic susceptibility. The resistivity measurement was conducted using a standard four-terminal method. The magnetic measurements were performed on a Magnetic Property Measurement System (MPMS-3, Quantum Design).

ARPES measurements

Synchrotron-based ARPES measurements were conducted at beamline 5-2 in Stanford synchrotron lightsource (SSRL, proposal No. S-XV-ST-

6370A). The samples were cleaved in-situ under ultra-high vacuum below 1×10^{-10} mbar. Data were collected with a Scienta DA30L electron analyzer. The total energy and angular resolutions were set to 15 meV and 0.2°, respectively. ARPES experiments were also repeated at beamline 03U and Dreamline in Shanghai Synchrotron Radiation Facility (SSRF).

Laser-ARPES measurements were conducted at Tsinghua University. The 7-eV laser was generated by frequency doubling in a KBBF crystal and focused on the sample by an optical lens with a beam spot of about 20 μm. $CsCr_3Sb_5$ single crystals were cleaved in-situ under ultra-high vacuum below 5×10^{-11} mbar. Data were collected by a Scienta DA30L electron analyzer. The total energy and angular resolutions were set to 3 meV and 0.2°, respectively.

DFT calculations

First-principles band structure calculations were performed using Vienna ab initio simulation package (VASP)[60] with a plane wave basis. The exchange-correlation energy was considered under Perdew-Burke-Ernzerhof (PBE) type generalized gradient approximation (GGA)[61] with spin-orbit coupling included. The cutoff energy for the plane-wave basis was set to 500 eV. A Γ-centered k-point mesh of 12 × 12 × 8 was adopted in the self-consistent calculations.

DFT + DMFT calculations

The single-site DFT + DMFT calculations are performed with full charge self-consistency using the DFT+eDMFT code[62,63] based on the WIEN2K package[64]. We choose a large hybridization energy window from -10 to 10 eV, including all the five correlated Cr 3*d* orbitals and other non-correlated orbitals such as Sb *p* orbitals, to capture the strong hybridization effect between the Sb *p* and Cr 3*d* orbitals. Rotationally-invariant local Coulomb interaction Hamiltonian is used, which is parameterized by on-site Hubbard U and Hund's coupling J_H. We choose the "exact" double-counting scheme[65]. The continuous-time quantum Monte Carlo (CTQMC)[66] is used as an impurity solver. The temperature for CTQMC is 100 K. The self-energy on real frequency is obtained by the analytical continuation method of maximum entropy.

Data availability

The data sets that support the findings of this study are available from the corresponding author upon request.

References

1. Balents, L. Spin liquids in frustrated magnets. *Nature* **464**, 199–208 (2010).
2. Fu, M., Imai, T., Han, T.-H. & Lee, Y. S. Evidence for a gapped spin-liquid ground state in a Kagome Heisenberg antiferromagnet. *Science* **350**, 655–658 (2015).
3. Yan, S., Huse, D. A. & White, S. R. Spin-liquid ground state of the *S* = 1/2 kagome Heisenberg antiferromagnet. *Science* **332**, 1173–1176 (2011).
4. Liu, D. F. et al. Magnetic Weyl semimetal phase in a Kagomé crystal. *Science* **365**, 1282–1285 (2019).
5. Liu, E. et al. Giant anomalous Hall effect in a ferromagnetic kagome-lattice semimetal. *Nat. Phys.* **14**, 1125–1131 (2018).
6. Morali, N. et al. Fermi-arc diversity on surface terminations of the magnetic Weyl semimetal $Co_3Sn_2S_2$. *Science* **365**, 1286–1291 (2019).
7. Ye, L. et al. Massive Dirac fermions in a ferromagnetic kagome metal. *Nature* **555**, 638–642 (2018).
8. Yin, J.-X. et al. Quantum-limit Chern topological magnetism in $TbMn_6Sn_6$. *Nature* **583**, 533–536 (2020).
9. Liu, Z., Liu, F. & Wu, Y.-S. Exotic electronic states in the world of flat bands: From theory to material. *Chin. Phys. B* **23**, 077308 (2014).
10. Tang, E., Mei, J.-W. & Wen, X.-G. High-temperature fractional quantum hall states. *Phys. Rev. Lett.* **106**, 236802 (2011).
11. Neupert, T., Santos, L., Chamon, C. & Mudry, C. Fractional quantum Hall states at zero magnetic field. *Phys. Rev. Lett.* **106**, 236804 (2011).
12. Ortiz, B. R. et al. New kagome prototype materials: discovery of KV_3Sb_5, RbV_3Sb_5, and CsV_3Sb_5. *Phys. Rev. Mater.* **3**, 094407 (2019).
13. Ortiz, B. R. et al. CsV_3Sb_5: A Z_2 Topological Kagome metal with a superconducting ground state. *Phys. Rev. Lett.* **125**, 247002 (2020).
14. Zhong, Y. et al. Testing electron–phonon coupling for the superconductivity in kagome metal CsV_3Sb_5. *Nat. Commun.* **14**, 1945 (2023).
15. Neupert, T. et al. Charge order and superconductivity in kagome materials. *Nat. Phys.* **18**, 137–143 (2022).
16. Kiesel, M. L., Platt, C. & Thomale, R. Unconventional Fermi surface instabilities in the Kagome Hubbard model. *Phys. Rev. Lett.* **110**, 126405 (2013).
17. Wang, W.-S., Li, Z.-Z., Xiang, Y.-Y. & Wang, Q.-H. Competing electronic orders on kagome lattices at van Hove filling. *Phys. Rev. B* **87**, 115135 (2013).
18. Teng, X. et al. Discovery of charge density wave in a kagome lattice antiferromagnet. *Nature* **609**, 490–495 (2022).
19. Wang, Q. et al. Large intrinsic anomalous Hall effect in half-metallic ferromagnet $Co_3Sn_2S_2$ with magnetic Weyl fermions. *Nat. Commun.* **9**, 3681 (2018).
20. Kang, M. et al. Dirac fermions and flat bands in the ideal kagome metal FeSn. *Nat. Mater.* **19**, 163–169 (2020).
21. Yin, J.-X. et al. Giant and anisotropic many-body spin–orbit tunability in a strongly correlated kagome magnet. *Nature* **562**, 91–95 (2018).
22. Gu, X. et al. Robust kagome electronic structure in the topological quantum magnets XMn_6Sn_6 (*X* = Dy, Tb, Gd, Y). *Phys. Rev. B* **105**, 155108 (2022).
23. Jiang, K. et al. Kagome superconductors AV_3Sb_5 (*A* = K, Rb, Cs). *Natl. Sci. Rev.* **10**, nwac199 (2023).
24. Zhao, H. et al. Cascade of correlated electron states in the kagome superconductor CsV_3Sb_5. *Nature* **599**, 216–221 (2021).
25. Nie, L. et al. Charge-density-wave-driven electronic nematicity in a kagome superconductor. *Nature* **604**, 59–64 (2022).
26. Wu, P. et al. Unidirectional electron–phonon coupling in the nematic state of a kagome superconductor. *Nat. Phys.* **19**, 1143–1149 (2023).
27. Jiang, Y.-X. et al. Unconventional chiral charge order in kagome superconductor KV_3Sb_5. *Nat. Mater.* **20**, 1353–1357 (2021).
28. Guo, C. et al. Switchable chiral transport in charge-ordered kagome metal CsV_3Sb_5. *Nature* **611**, 461–466 (2022).
29. Le, T. et al. Superconducting diode effect and interference patterns in kagome CsV_3Sb_5. *Nature* **630**, 64–69 (2024).
30. Li, H. et al. Unidirectional coherent quasiparticles in the high-temperature rotational symmetry broken phase of AV_3Sb_5 kagome superconductors. *Nat. Phys.* **19**, 637–643 (2023).
31. Mielke, C. et al. Time-reversal symmetry-breaking charge order in a kagome superconductor. *Nature* **602**, 245–250 (2022).
32. Yang, S.-Y. et al. Giant, unconventional anomalous Hall effect in the metallic frustrated magnet candidate, KV_3Sb_5. *Sci. Adv.* **6**, eabb6003 (2020).
33. Chen, H. et al. Roton pair density wave in a strong-coupling kagome superconductor. *Nature* **599**, 222–228 (2021).
34. Li, H. et al. Small Fermi pockets intertwined with charge stripes and pair density wave order in a kagome superconductor. *Phys. Rev. X* **13**, 031030 (2023).

35. Li, H., Kim, Y. B. & Kee, H.-Y. Intertwined van Hove singularities as a mechanism for loop current order in Kagome metals. *Phys. Rev. Lett.* **132**, 146501 (2024).
36. Tazai, R., Yamakawa, Y. & Kontani, H. Charge-loop current order and Z_3 nematicity mediated by bond order fluctuations in kagome metals. *Nat. Commun.* **14**, 7845 (2023).
37. Feng, X., Jiang, K., Wang, Z. & Hu, J. Chiral flux phase in the Kagome superconductor AV_3Sb_5. *Sci. Bull.* **66**, 1384–1388 (2021).
38. Hu, Y. et al. Rich nature of Van Hove singularities in Kagome superconductor CsV_3Sb_5. *Nat. Commun.* **13**, 2220 (2022).
39. Kang, M. et al. Twofold van Hove singularity and origin of charge order in topological kagome superconductor CsV_3Sb_5. *Nat. Phys.* **18**, 301–308 (2022).
40. Hu, Y. et al. Topological surface states and flat bands in the kagome superconductor CsV_3Sb_5. *Sci. Bull.* **67**, 495–500 (2022).
41. Liu, Y. et al. Superconductivity under pressure in a chromium-based kagome metal. *Nature* **632**, 1032–1037 (2024).
42. Xu, C. et al. Frustrated altermagnetism and charge density wave in Kagome superconductor $CsCr_3Sb_5$. Preprint at https://doi.org/10.48550/arXiv.2309.14812 (2024).
43. Wu, S. et al. Flat-band enhanced antiferromagnetic fluctuations and unconventional superconductivity in pressurized $CsCr_3Sb_5$. *Nat. Commun.* **16**, 1375 (2025).
44. Aoki, H. Theoretical possibilities for flat band superconductivity. *J. Supercond. Nov. Magn.* **33**, 2341–2346 (2020).
45. Wang, Y. Heavy-fermions in frustrated Hund's metal with portions of incipient flat-bands. *Phys. Rev. B* **111**, 035127 (2025).
46. Fang, X. et al. Electron correlations in the kagome flat band metal $CsCr_3Sb_5$. Preprint at https://doi.org/10.48550/arXiv.2403.03911 (2024).
47. Kuroki, K., Higashida, T. & Arita, R. High-T_C superconductivity due to coexisting wide and narrow bands: A fluctuation exchange study of the Hubbard ladder as a test case. *Phys. Rev. B* **72**, 212509 (2005).
48. Linscheid, A. et al. High T_C via Spin fluctuations from incipient bands: Application to monolayers and intercalates of FeSe. *Phys. Rev. Lett.* **117**, 077003 (2016).
49. Kato, T. et al. Polarity-dependent charge density wave in the kagome superconductor CsV_3Sb_5. *Phys. Rev. B* **106**, L121112 (2022).
50. Yi, M. et al. Observation of temperature-induced crossover to an orbital-selective mott phase in $A_xFe_{2-y}Se_2$ (A = K, Rb) superconductors. *Phys. Rev. Lett.* **110**, 067003 (2013).
51. Lanatà, N. et al. Orbital selectivity in Hund's metals: The iron chalcogenides. *Phys. Rev. B* **87**, 045122 (2013).
52. Hardy, F. et al. Evidence of strong correlations and coherence-incoherence crossover in the iron pnictide superconductor KFe_2AS_2. *Phys. Rev. Lett.* **111**, 027002 (2013).
53. Yang, J. et al. Orbital-dependent electron correlation in double-layer nickelate $La_3Ni_2O_7$. *Nat. Commun.* **15**, 4373 (2024).
54. Li, Y. et al. Electronic correlation and pseudogap-like behavior of high-temperature superconductor $La_3Ni_2O_7$. *Chin. Phys. Lett.* **41**, 087402 (2024).
55. Sun, H. et al. Signatures of superconductivity near 80 K in a nickelate under high pressure. *Nature* **621**, 493–498 (2023).
56. Zhu, Y. et al. Superconductivity in pressurized trilayer $La_4Ni_3O_{10-\delta}$ single crystals. *Nature* **631**, 531–536 (2024).
57. Yucheng, G. et al. Ubiquitous flat bands in a Cr-based Kagome superconductor. Preprint at https://doi.org/10.48550/arXiv.2406.05293 (2024).
58. Shuting, P. et al. Flat bands and distinct density wave orders in correlated Kagome superconductor $CsCr_3Sb_5$. Preprint at https://doi.org/10.48550/arXiv.2406.17769 (2024).
59. Suzuki, S. et al. Evolution of band structure in the kagome superconductor $Cs(V_{1-x}Cr_x)_3Sb_5$: Toward universal understanding of charge density wave and superconducting phase diagrams. *Phys. Rev. B* **110**, 165104 (2024).
60. Kresse, G. & Furthmüller, J. Efficient iterative schemes for ab initio total-energy calculations using a plane-wave basis set. *Phys. Rev. B* **54**, 11169–11186 (1996).
61. Perdew, J. P., Burke, K. & Ernzerhof, M. Generalized gradient approximation made simple. *Phys. Rev. Lett.* **77**, 3865–3868 (1996).
62. Haule, K., Yee, C.-H. & Kim, K. Dynamical mean-field theory within the full-potential methods: Electronic structure of $CeIrIn_5$, $CeCoIn_5$, and $CeRhIn_5$. *Phys. Rev. B* **81**, 195107 (2010).
63. Haule, K. & Birol, T. Free energy from stationary implementation of the DFT+DMFT functional. *Phys. Rev. Lett.* **115**, 256402 (2015).
64. Blaha, P. et al. WIEN2k: An APW+lo program for calculating the properties of solids. *J. Chem. Phys.* **152**, 074101 (2020).
65. Haule, K. Exact double counting in combining the dynamical mean field theory and the density functional theory. *Phys. Rev. Lett.* **115**, 196403 (2015).
66. Gull, E. et al. Continuous-time Monte Carlo methods for quantum impurity models. *Rev. Mod. Phys.* **83**, 349–404 (2011).

Acknowledgements

We thank D.W. Shen, Z.T. Liu, and Y.B. Huang for the access to the beamline 03U and the Dreamline at SSRF. This work is funded by the National Key R&D Program of China (Grant No. 2022YFA1403200, 2022YFA1403100, 2023YFA1406101, and 2022YFA1604400/03) and the National Natural Science Foundation of China (No. 92365204, No. 12274251, and No. 12274298). L.X.Y. acknowledges the Fund of Science and Technology on Surface Physics and Chemistry Laboratory (No. XKFZ202102). Y.L.W. was supported by the National Natural Science Foundation of China (No. 12174365), the New Cornerstone Science Foundation, and the Innovation Program for Quantum Science and Technology (No. 2021ZD0302800). Use of the Stanford Synchrotron Radiation Lightsource, SLAC National Accelerator Laboratory, is supported by the U.S. Department of Energy, Office of Science, Office of Basic Energy Sciences under Contract No. DE-AC02-76SF00515.

Author contributions

L.X.Y. and G.H.C. conceived the experiments. Y.D.L. carried out ARPES measurements with the assistance of X.D., W.X.Z., K.Y.Z., Y.Q.H., S.Y.Z., H.K.C., J.Y.L., C.P., Y.H.Y., D.H.L., M.H., Z.K.L., and Y.L.C. Ab-initio calculations were performed by X.D. and S.Q.W. DFT + DMFT calculations were performed by Y.L.W. Single crystals were synthesized and characterized by Y.L. and G.H.C. The paper was written by Y.D.L. and L.X.Y. All authors contributed to the scientific planning and discussion.

Competing interests

The authors declare that they have no competing interests.

Additional information

Supplementary information The online version contains supplementary material available at https://doi.org/10.1038/s41467-025-58487-x.

Correspondence and requests for materials should be addressed to Yilin Wang, Yulin Chen, Guanghan Cao or Lexian Yang.

Peer review information *Nature Communications* thanks the anonymous reviewers for their contribution to the peer review of this work. A peer review file is available.